Emergent Symmetry and Valley Chern Insulator in Twisted Double-Bilayer Graphene

Yimeng Wang[,1] G. William Burg[,1] Biao Lian,[2] Kenji Watanabe[,3] Takashi Taniguchi[,4]
B. Andrei Bernevig,[5] and Emanuel Tutuc[1,*]

[1]*Microelectronics Research Center, Department of Electrical and Computer Engineering,*
The University of Texas at Austin, Austin, Texas 78758, USA
[2]*Princeton Center for Theoretical Science, Princeton University, Princeton, New Jersey 08544, USA*
[3]*Research Center for Functional Materials, National Institute of Materials Science, 1-1 Namiki Tsukuba, Ibaraki 305-0044, Japan*
[4]*International Center for Materials Nanoarchitectonics, National Institute of Materials Science,*
1-1 Namiki Tsukuba, Ibaraki 305-0044, Japan
[5]*Department of Physics, Princeton University, Princeton, New Jersey 08544, USA*

Theoretical calculations show that twisted double bilayer graphene (TDBG) under a transverse electric field develops a valley Chern number 2 at charge neutrality. Using thermodynamic and thermal activation measurements we report the experimental observation of a universal closing of the charge neutrality gap in the Hofstadter spectrum of TDBG at $1/2$ magnetic flux per unit cell, in agreement with theoretical predictions for a valley Chern number 2 gap. Our theoretical analysis of the experimental data shows that the interaction energy, while larger than the flat-band bandwidth in TDBG near $1°$ does not alter the emergent valley symmetry or the single-particle band topology.

Moiré patterns of two-dimensional (2D) materials provide a highly tunable platform for exploring correlated electronic states in electronic bands with flat dispersion. Celebrated examples include the twisted bilayer graphene (TBG) at the magic angle $\theta \simeq 1.1°$ [1–5], twisted double-bilayer graphene [6–9], ABC trilayer graphene on hexagonal boron-nitride (hBN) [10,11], twisted trilayer graphene [12–15], as well as fractional Chern insulators in twisted bilayer $MoTe_2$ [16–18] and pentalayer rhombohedral graphene on hBN [19], all of which exhibit superconducting or correlated insulator phases. Theoretical calculations show that a new emergent symmetry—which decouples two originally strongly intertwined valleys [1]—appears, and that, per each of the two valley emergent symmetry sectors, the electron bands of many moiré systems are topologically nontrivial. For example, twisted double bilayer graphene (TDBG) and ABC trilayer graphene on hBN carry nonzero emergent-valley Chern numbers 2 and 3, respectively, under a transverse electric field [20–25]. Unlike correlated Chern insulators induced by interactions in the flat moiré bands, the valley Chern insulators in these systems stem from the nontrivial band topology protected by time-reversal invariance.

Experimental signatures of nontrivial band topology include transport experiments of the quantum spin Hall effect in 2D time-reversal invariant systems [26], the quantum anomalous Hall effect of Chern insulators in magnetic topological insulator thin films [27], and the

angle-resolved photoemission spectroscopy and scanning tunneling microscope studies of 3D time-reversal invariant topological insulators [28–30]. In TDBG under transverse electric field the gap at charge neutrality carries a topological valley Chern number $C_V = 2$, protected by an emergent valley U(1) symmetry [20–23,25]. This emergent symmetry may be broken on the edge, leading to backscattering between the counterpropagating edge states from different valleys. Although interactions may drive moiré systems into a correlated Chern insulator with protected edge states [17–19,31–34], such state is not necessarily related to the noninteracting band topology protected by the emergent valley symmetry. A bulk measurement of the band topological character per emergent symmetry sector (valley) is therefore necessary.

Theoretical studies suggest that the nontrivial band topology manifests itself in the Hofstadter butterfly, and can be observed through bulk magnetotransport [35–39]. In particular, a noninteracting band gap that carries a topological valley Chern number $C_V > 0$ is predicted to close at or before magnetic flux per unit cell $\Phi = (1/C_V)\Phi_0$ ($\Phi_0 = h/e$ is the flux quanta). Here, we present a combined experimental and theoretical study of magnetotransport in TDBG at $\theta = 0.97°$, $1.01°$, and $1.33°$. As a function of perpendicular magnetic field (B) the experimental data show an unexpected closing of the gap at charge neutrality when the flux per moiré unit cell $\Phi \approx (1/2)\Phi_0$ or smaller, in contrast with the tenets of the quantum Hall effect, which dictate that gaps increase as a function of B. This observation is consistent with the valley Chern number

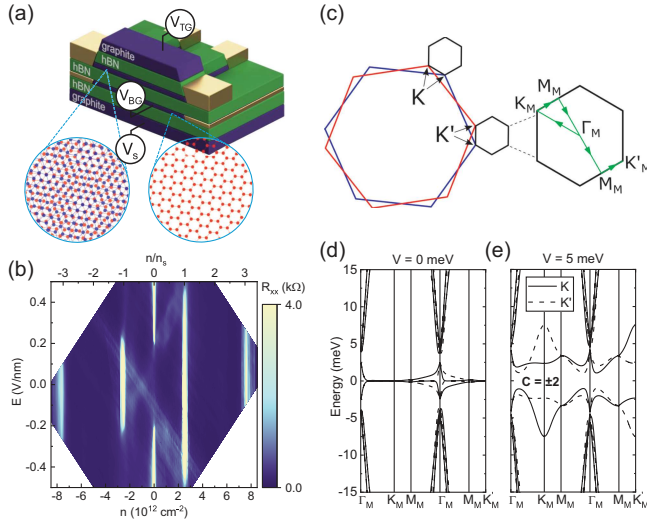*Contact author: etutuc@mail.utexas.edu

FIG. 1. (a) TDBG sample schematic with graphite top gate and graphene bottom gate. For chemical potential measurements the bottom gate is made of monolayer graphene and has multiple contacts. A substrate gate below the bottom gate is used to tune the E-field at which the chemical potential is measured. (b) Contour plot of R_{xx} vs n and E measured in the TDBG sample with $\theta = 1.01°$ at $T = 1.5$ K. The top axis shows n in units of n_s. (c) Decoupled moiré Brillouin zones arise at the K and K' points of the graphene bilayers. The enlarged view of the moiré Brillouin zone shows the high symmetry points and the path taken in momentum space for the (d),(e) calculations. (d), (e) Calculated moiré band structures at (d) $V = 0$ and (e) $V = 5$ meV. Solid (dashed) lines represent the moiré bands in the K (K') valleys of the graphene bilayers. At finite V, the gap at charge neutrality has Chern numbers $+2$ and -2 in the K and K' valleys, respectively.

$C_V = 2$ of the valley-filtered flat bands, which supports both the band topology and the emergent symmetry that protects it. Furthermore, by theoretically analyzing the effect of interactions, we show that our experiment implies an interaction energy scale larger than the bandwidth of the flat bands in TDBG at $\theta = 1.01°$, and that the interaction does not spoil the single-particle band topology and the emergent valley symmetry at charge neutrality.

Figure 1(a) shows a schematic of the TDBG sample, with hBN dielectrics and three gates—top, bottom, and substrate gates. The top and the bottom gates are used to independently control the carrier density (n) and transverse electric field (E) in the TDBG. For the $\theta = 0.97°$ sample the bottom gate, which is made of monolayer graphene and contacted with several electrodes, also acts as a resistively detected Kelvin probe to the TDBG chemical potential. The substrate gate is added to the dual gated geometry to tune the transverse E-field at which the TDBG chemical potential is measured [34].

Figure 1(b) shows the longitudinal resistance (R_{xx}) as a function of n and E in a TDBG sample with $\theta = 1.01°$. The twist angle is defined such that in the limit $\theta = 0°$ the

TDBG approaches AB-AB stacking [Fig. 1(c)]. R_{xx} maxima along lines of constant n indicate energy gaps in the moiré band structure. The data show E-dependent gaps at charge neutrality ($n = 0$) and at fixed densities $\pm n_s$ and $\pm 3n_s$. Here, n_s is the carrier density required to fill a moiré unit cell with fourfold spin-valley degeneracy, and is related to the twist angle by

$$n_s = 4 \frac{2}{\sqrt{3}} \left[\frac{\sin(\frac{\theta}{2})}{(a/2)} \right]^2;$$

$a = 2.46$ Å is the graphene lattice constant. At charge neutrality, the band gap is initially small and increases with E, while the gaps at $\pm n_s$ decrease and eventually close at finite E. In addition, there are emerging R_{xx} maxima at $n = +\frac{1}{2}n_s$ within small windows of E around ± 0.3 V/nm, corresponding to developing correlated insulators at half-filling of the first conduction moiré band. Correlated insulators appear at half and quarter moiré band filling in TDBG flat bands as a result of strong electron-electron interaction [6–9,40].

For small θ the TDBG moiré pattern reciprocal vector is much smaller than the intervalley momentum difference, which leads to distinct moiré Brillouin zones at the K and K' valleys of the parent graphene bilayers that are exponentially (in $1/\theta$) decoupled from one another [Fig. 1(c)]. This decoupling gives the moiré bands a valley degree of freedom, and an emergent valley U(1) rotation symmetry. Figures 1(d) and 1(e) show $\theta = 1.01°$ band structure calculations for zero and finite on-site energy difference (V) between neighboring graphene layers, respectively, and demonstrate the valley dependence of the bands. The V values are proportional to the applied transverse electric field E [41]. Furthermore, the calculated V dependence is consistent with experimental observations, showing that the gap at charge neutrality opens with increasing E, and the gaps between the first and second moiré bands reduce or close.

At finite V, the gap that opens at charge neutrality is predicted to be topologically nontrivial [20–23,25], with a valley-dependent Chern number of $C_K = +2$ or $C_{K'} = -2$ [Fig. 1(e)], which originates from the opening of two double Dirac cones of the same helicity in each valley. The gap thus carries a valley Chern number $C_V = (C_K - C'_K)/2 = 2$ per spin, protected by the emergent valley U(1) symmetry, a bulk symmetry that can be broken by edge roughness. Instead, we explore here bulk signatures of the nonzero valley Chern number by examining the magneto-transport of TDBG in perpendicular magnetic fields, with an emphasis on the gap at charge neutrality. Figure 2(a) shows R_{xx} as a function of n and B for $E = 0.31$ V/nm in $\theta = 1.01°$ TDBG. The combination of perpendicular magnetic fields and the spatial modulation of the moiré pattern leads to equally spaced Landau levels in the energy spectrum, and quantum Hall states (QHSs) when n and Φ satisfy the Streda formula [46,47]:
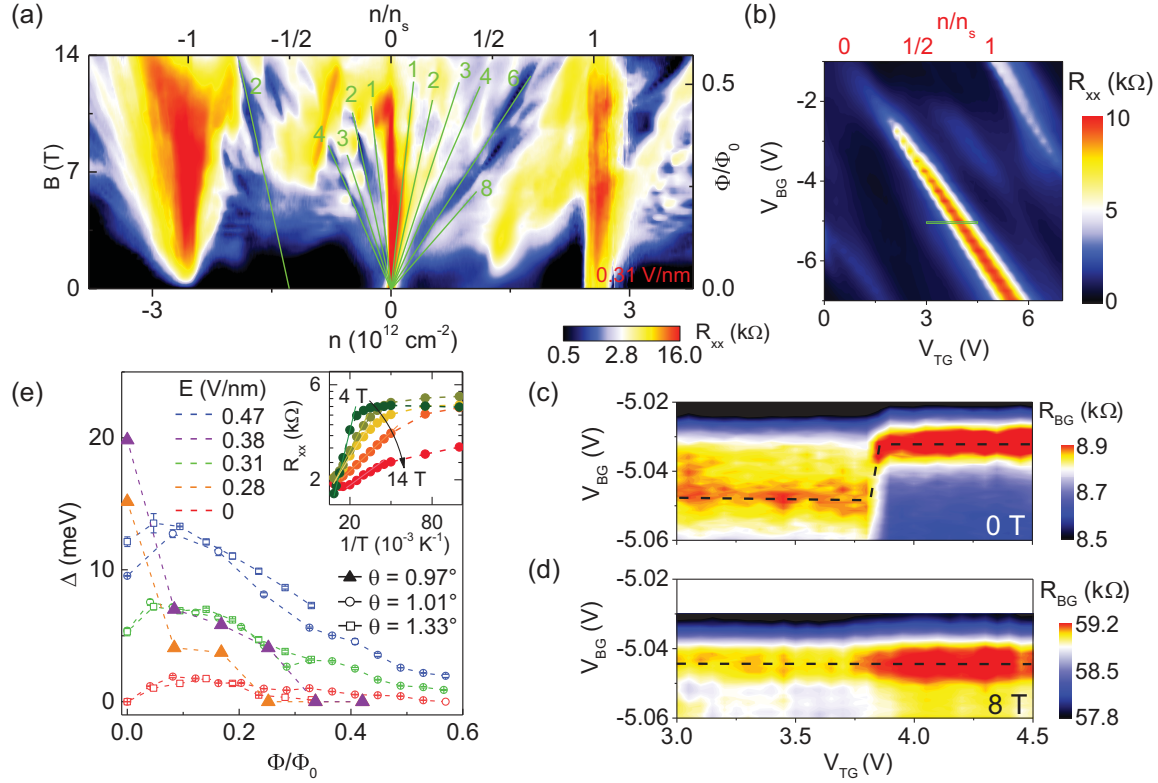
FIG. 2. (a) R_{xx} vs n and B at $E = 0.31$ V/nm for TDBG with $\theta = 1.01°$. The top axis shows n in units of n_s, and the right axis shows Φ/Φ_0. The Landau level filling factor for well-developed quantum Hall states are labeled. (b) R_{xx} vs V_{TG} and V_{BG} for the $\theta = 0.97°$ TDBG. The top axis shows n/n_s for the diagonal resistance maxima. (c),(d) R_{BG} vs V_{TG} and V_{BG} measured at (c) $B = 0$ T and (d) 8 T. Black dashed lines mark charge neutrality loci of the bottom gate graphene. Data are taken at $T = 1.5$ K in (a)–(d). (e) Δ vs Φ/Φ_0 at different E fields for three TDBG samples. The triangles represent thermodynamic measurements in the $\theta = 0.97°$ TDBG; the circles and squares represent thermal activation measurements in the $\theta = 1.01°$ and 1.33° TDBGs. Inset shows Arrhenius plot of R_{xx} vs $1/T$ at charge neutrality for $E = 0.47$ V/nm, and at different B-fields for the $\theta = 1.01°$ TDBG.

$$\frac{n}{n_s} = \frac{\nu}{4}\frac{\Phi}{\Phi_0} + \sigma,$$

where $\Phi = BA_M$, $A_M = 4/n_s$ is the moiré unit cell area, and ν and σ are Landau level and moiré band filling factors, respectively. The best developed QHSs are labeled by their corresponding ν value in Fig. 2(a). An advantage of small twist angle TDBG is the large unit cell area, which makes high magnetic flux values relatively easy to access experimentally. As shown on the right axes of Fig. 2(a), Φ/Φ_0 exceeds $1/2$ at $B = 14$ T, values at which the predicted topological signatures should manifest.

Focusing now on the Φ/Φ_0 dependence of the gap at charge neutrality, Fig. 2(a) shows that R_{xx} at charge neutrality is initially large, and generally independent of B for low and moderate fields, but then decreases as Φ/Φ_0 approaches $1/2$. While resistance is not necessarily a direct measure of an energy gap, especially when topological edge states may be present, these findings suggest that the gap at charge neutrality decreases at high magnetic flux in the vicinity of $\Phi/\Phi_0 = 1/2$. To substantiate this finding, a bulk measurement is needed. To that end, we measure the gap (Δ) at charge neutrality as a function of Φ/Φ_0 using a combination of thermodynamic measurements and thermal activation. Figures 2(b)–2(d) show the thermodynamic measurements in the $\theta = 0.97°$ TDBG. In Fig. 2(b), R_{xx} as a function of V_{TG} and V_{BG} is shown, where the resistance maxima along the diagonal represent the TDBG charge neutrality. Figure 2(c) shows the resistance of the graphene bottom gate R_{BG} as a function of V_{TG} and V_{BG} measured at $E = 0.38$ V/nm and $B = 0$ T. The R_{BG} is measured around the TDBG charge neutrality in the range marked by the green rectangle in Fig. 2(b), with the substrate gate at a fixed bias to shift the neutrality point of the bottom gate graphene to the target E-field. As detailed in Ref. [34], by tracing the charge neutrality of the bottom gate graphene, the chemical potential of the TDBG can be measured directly, revealing the bulk properties at charge neutrality. Specifically, the chemical potential of the TDBG can be calculated with $\mu = eV_{BG}(1 + C_s/C_{BG}) - eV_sC_s/C_{BG}$. Here, C_{BG} and C_s are the capacitance per unit area of the bottom and substrate gate dielectric,

respectively, and V_s is the substrate gate bias. Accordingly, the change of μ is proportional to the change of V_{BG} when tracing the bottom gate charge neutrality plotted in Fig. 2(c), and the step the charge neutrality loci take at $V_{BG} \approx 3.8$ V reflects the TDBG thermodynamic gap at its charge neutrality, which is $\Delta = 20$ meV. The data for the same measurement at $B = 8$ T are shown in Fig. 2(d), where no gap is observed. The values of Δ vs Φ/Φ_0 measured in the $\theta = 0.97°$ TDBG at fixed E-field values are shown in Fig. 2(e) (triangle symbols). Meanwhile, we perform thermal activation measurements on the $\theta = 1.01°$ and $1.33°$ TDBGs [Fig. 2(e) inset], and summarize the thermodynamic and activation measurement results of Δ vs Φ/Φ_0 in Fig. 2(e). Although differences exist between datasets, in both types of measurements the charge neutrality gap shows a closing behavior near or before $\Phi/\Phi_0 = 1/2$, which suggests a common origin of the gap closing. In the $\theta = 1.33°$ TDBG, Δ shows a similar decreasing trend, but is only measurable up to $\Phi/\Phi_0 \simeq 0.3$ due to the larger twist angle.

The observations in Fig. 2 are surprising. For typical band structures energy gaps are expected to open with increasing B. In magic angle TBG, a similar system with flat bands and strong interactions, compressibility measurements reveal the charge neutrality gap increases with B [48]. Consequently, as we explain below, the observed gap closing near $\Phi/\Phi_0 = 1/2$ is compelling evidence of the nontrivial topology of charge neutrality gap in TDBG, and of the emergent symmetry that protects the valley Chern number. It is important to distinguish between the valley Chern insulator in TDBG, and the correlated Chern insulators in TBG that break time reversal symmetry [49–51]. The fillings of the latter disperse in a perpendicular magnetic field according to the Streda formula [46,47], similar to a quantum Hall state. The valley Chern gap in TDBG does not break time reversal symmetry, and is not expected to disperse according to the Streda formula.

In the noninteracting band theory, the Hofstadter spectrum of a trivial band is usually bounded within its bandwidth, leaving the gap between topologically trivial bands open at any Φ/Φ_0 as shown in Fig. 3(a) [41]. In contrast, a topological gap will generically close at a certain magnetic flux, connecting the Hofstadter spectra above and below the gap. The simplest example is a Chern number C gap between two Chern bands of Chern numbers $\pm C$, which is topologically enforced to close at $\Phi/\Phi_0 = 1/|C|$ [35,38,39,41]. Two examples of Chern number $C = 1$ and $C = 2$ gaps are shown in Figs. 3(b) and 3(c), respectively [41].

In TDBG with nonzero V, each valley has a Chern number ± 2 gap at charge neutrality, which is forced to close at $\Phi/\Phi_0 = 1/2$. Figures 3(d) and 3(e) show the Hofstadter butterflies at valley K and K' calculated [35,38] using the noninteracting TDBG continuum model at $\theta = 1.01°$ and $V = 5$ meV. The spectra of the lowest two moiré

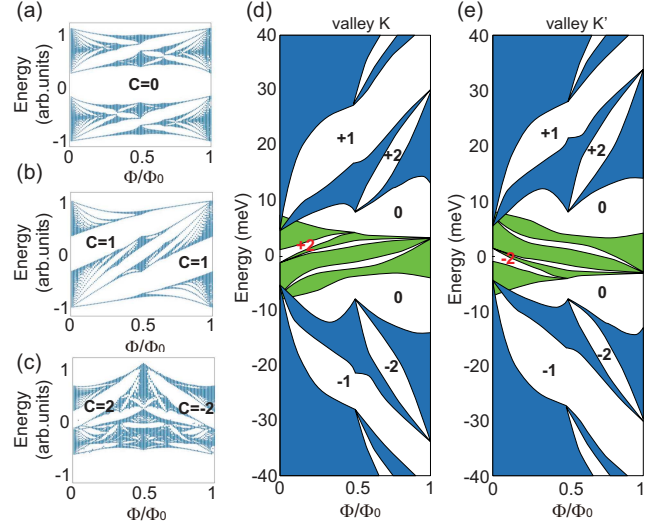

FIG. 3. (a)–(c) Hofstadter butterflies of two-band Chern insulator tight-binding models with Chern numbers 0,1, and 2, respectively. A gap of Chern number C is topologically protected to close at $\Phi/\Phi_0 = 1/C$. (d),(e) The Hofstadter spectra of TDBG with $\theta = 1.01°$ and $V = 5$ meV at valleys K and K', respectively. The spectra include the lowest two moiré bands (green) and the higher moiré bands (blue). The integers label the Chern numbers of the dominant Hofstadter gaps.

bands are shown in green. As expected, at $\Phi/\Phi_0 = 1/2$, the Chern number $C_K = 2$ ($C_{K'} = -2$) charge neutrality gap of valley K (K') closes at the top (bottom) of the lowest two moiré bands. Figure 4(a) shows the single valley gap with respect to Φ/Φ_0 at different V. This strongly suggests that the experimentally observed charge neutrality gap
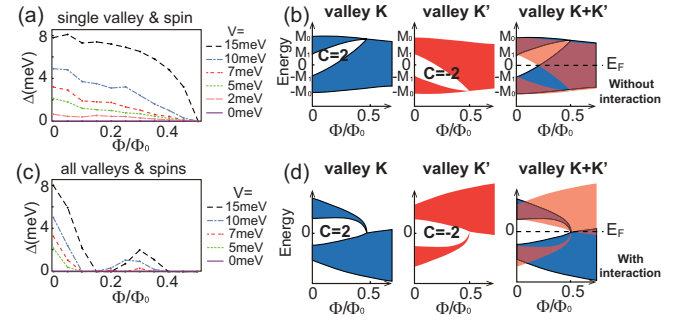

FIG. 4. (a) The $C_\eta = \pm 2$ Chern gap of a single valley and spin vs Φ/Φ_0. (b) Schematics of the noninteracting Hofstadter spectra at valley K and K'. The $C_\eta = \pm 2$ Chern gaps of the two valleys ($\eta = \pm 1$ for valleys K and K', respectively) split in energy at finite magnetic field, leading to a total charge neutrality gap closing before $\Phi/\Phi_0 = 1/2$. (c) The total noninteracting charge neutrality gap of all spins and valleys of TDBG vs Φ/Φ_0, where the spin g-factor 2 is used. (d) Illustration of the effective Hofstadter spectra under interaction by mean field theory, where the $C_\eta = \pm 2$ Chern gaps of valleys K and K' are enlarged and shifted towards each other, leading to a total charge neutrality gap closing around $\Phi/\Phi_0 = 1/2$.

closing at $\Phi/\Phi_0 = 1/2$ in TDBG is due to the valley-dependent Chern number $C_K = -C_{K'} = 2$.

However, the midgap energies of the $C_K = 2$ and $C_{K'} = -2$ Chern gaps at valleys K and K' disperse oppositely with Φ, which differ by ~ 10 meV at $\Phi/\Phi_0 = 1/2$ [Figs. 3(d) and 3(e)]. Furthermore, the Zeeman spin splitting is ~ 1 meV at $\Phi/\Phi_0 = 1/2$. Therefore, the total single-particle valley Chern gap of all spins and valleys at charge neutrality would close before $\Phi/\Phi_0 = 1/2$ due to energy band overlaps, as illustrated in Fig. 4(b). The calculated total valley Chern gap Δ of all spins and valleys for TDBG at $\theta = 1.01°$ and different V closes no later than $\Phi/\Phi_0 \approx 0.2$ [Fig. 4(c)], and shows a gap reopening around $0.2 < \Phi/\Phi_0 < 0.4$ due to other, further, Landau level gaps, different from our experimental observation. This discrepancy can be resolved by considering electron-electron interactions, which we treat here in a mean-field theory. Denote the bottom and top of the first conduction (valence) moiré band at $\Phi = 0$ as M_1 ($-M_0$) and M_0 ($-M_1$), respectively, as shown in Fig. 4(b) ($M_0 > M_1 > 0$). For simplification, we assume the Chern gap of valley η (+1 for K and -1 for K') decreases linearly and closes at energy ηM_0 at $\Phi/\Phi_0 = 1/2$. The number of conduction (valence) states per area above (below) the gap at valley η and spin s is given by $N_{m,\eta}(\Phi) = (1 - 2m\eta\Phi/\Phi_0)/A_M$ ($m = \pm 1$ for conduction and valence bands, respectively).

We consider a local interaction particle-hole symmetric about charge neutrality:

$$\mathcal{H}_I = \frac{U_0 A_M}{2} \sum_{m,m',\eta,\eta',s,s'} \gamma_{m\eta s}^{m'\eta's'}(\Phi)\tilde{n}_{m,\eta,s}\tilde{n}_{m',\eta',s'},$$

where $U_0 > 0$ is the short-range interaction energy, $\tilde{n}_{m,\eta,s} = n_{m,\eta,s} - [N_{m,\eta}(\Phi)/2]$ is the electron density of indices $\{m, \eta, s\}$ relative to half-filling, with $0 \le n_{m,\eta,s} \le N_{m,\eta}(\Phi)$, and $\gamma_{m\eta s}^{m'\eta's'}(\Phi) = 1 - \delta_{m,m'}\delta_{\eta,\eta'}\delta_{s,s'} - \delta_{m,-m'}\delta_{\eta,\eta'}\delta_{s,s'}\zeta(\Phi)$ accounts for reduced interaction within the same valley and spin due to Pauli exclusion [41]. We assume each band $\{m, \eta, s\}$ has a uniform density of states. This allows us to calculate the total mean-field energy at the filling of charge neutrality, and derive the ground-state charge neutrality gap $\Delta(\Phi)$ with respect to Φ [41]. We find two interaction effects: first, the charge neutrality gap at $\Phi = 0$ increases from the single-particle gap $2M_1$ to $\Delta(0) = 2M_1 + U_0$. Second, the charge-neutrality valley Chern gap $\Delta(\Phi)$ closes at $\Phi/\Phi_0 = [(2M_1 + U_0)/(4M_0 + 4M_1 - 2U_0)] < 1/2$ for weak interactions $0 < U_0 < M_0$ (but is larger than noninteracting cases), while the gap closes at $\Phi/\Phi_0 \approx 1/2$ for strong interactions $U_0 \ge M_0$, analogous to the single valley gap in Fig. 4(a). Heuristically, this is because the interaction increases the energy cost for a valence electron to jump into a conduction band, stabilizing the charge neutrality gap. In the mean-field picture, the bands of the two valleys are effectively deformed by interaction as shown in Fig. 4(d), with their Chern gaps enlarged and shifted towards each other. Such a simplified mean field picture is further verified by our numerical Hartree-Fock calculation of the Hofstadter spectrum of a valley Chern number 2 tight-binding model with on-site Hubbard interactions [41].

Our experimental observations reveal the TDBG charge neutrality gap under a transverse E-field shows an unusual closing in the presence of a perpendicular magnetic field, consistent with a valley Chern insulator with $C_V = 2$. Moreover, the interaction energy U_0, although larger than the flat band widths in TDBG near $\theta = 1°$, preserves the emergent valley U(1) symmetry and the valley Chern number. Our study provides a novel method to detect the band topology of 2D moirés and other superlattice systems by measurement of their bulk energy spectra.

[1] R. Bistritzer and A. H. MacDonald, Proc. Natl. Acad. Sci. U.S.A. **108**, 12233 (2011).

[2] Y. Cao, V. Fatemi, S. Fang, K. Watanabe, T. Taniguchi, E. Kaxiras, and P. Jarillo-Herrero, Nature (London) **556**, 43 (2018).

[3] Y. Cao, V. Fatemi, A. Demir, S. Fang, S. L. Tomarken, J. Y. Luo, J. D. Sanchez-Yamagishi, K. Watanabe, T. Taniguchi, E. Kaxiras, R. C. Ashoori, and P. Jarillo-Herrero, Nature (London) **556**, 80 (2018).

[4] M. Yankowitz, S. Chen, H. Polshyn, Y. Zhang, K. Watanabe, T. Taniguchi, D. Graf, A. F. Young, and C. R. Dean, Science **363**, 1059 (2019).

[5] X. Lu, P. Stepanov, W. Yang, M. Xie, M. A. Aamir, I. Das, C. Urgell, K. Watanabe, T. Taniguchi, G. Zhang, A. Bachtold, A. H. MacDonald, and D. K. Efetov, Nature (London) **574**, 653 (2019).

[6] X. Liu, Z. Hao, E. Khalaf, J. Y. Lee, Y. Ronen, H. Yoo, D. Haei Najafabadi, K. Watanabe, T. Taniguchi, A. Vishwanath, and P. Kim, Nature (London) **583**, 221 (2020).

[7] G. W. Burg, J. Zhu, T. Taniguchi, K. Watanabe, A. H. MacDonald, and E. Tutuc, Phys. Rev. Lett. **123**, 197702 (2019).

[8] C. Shen, Y. Chu, Q. Wu, N. Li, S. Wang, Y. Zhao, J. Tang, J. Liu, J. Tian, K. Watanabe, T. Taniguchi, R. Yang, Z. Y. Meng, D. Shi, O. V. Yazyev, and G. Zhang, Nat. Phys. **16**, 520 (2020).

[9] Y. Cao, D. Rodan-Legrain, O. Rubies-Bigorda, J. M. Park, K. Watanabe, T. Taniguchi, and P. Jarillo-Herrero, Nature (London) **583**, 215 (2020).

[10] G. Chen, L. Jiang, S. Wu, B. Lyu, H. Li, B. L. Chittari, K. Watanabe, T. Taniguchi, Z. Shi, J. Jung, Y. Zhang, and F. Wang, Nat. Phys. **15**, 237 (2019).

[11] G. Chen, A. L. Sharpe, P. Gallagher, I. T. Rosen, E. J. Fox, L. Jiang, B. Lyu, H. Li, K. Watanabe, T. Taniguchi, J. Jung, Z. Shi, D. Goldhaber-Gordon, Y. Zhang, and F. Wang, Nature (London) **572**, 215 (2019).

[12] J. M. Park, Y. Cao, K. Watanabe, T. Taniguchi, and P. Jarillo-Herrero, Nature (London) **590**, 249 (2021).

[13] Z. Hao, A. M. Zimmerman, P. Ledwith, E. Khalaf, D. H. Najafabadi, K. Watanabe, T. Taniguchi, A. Vishwanath, and P. Kim, Science **371**, 1133 (2021).

[14] Y. Cao, J. M. Park, K. Watanabe, T. Taniguchi, and P. Jarillo-Herrero, Nature (London) **595**, 526 (2021).

[15] H. Kim, Y. Choi, C. Lewandowski, A. Thomson, Y. Zhang, R. Polski, K. Watanabe, T. Taniguchi, J. Alicea, and S. Nadj-Perge, Nature (London) **606**, 494 (2022).

[16] Y. Zeng, Z. Xia, K. Kang, J. Zhu, P. Knüppel, C. Vaswani, K. Watanabe, T. Taniguchi, K. F. Mak, and J. Shan, Nature (London) **622**, 69 (2023).

[17] J. Cai, E. Anderson, C. Wang, X. Zhang, X. Liu, W. Holtzmann, Y. Zhang, F. Fan, T. Taniguchi, K. Watanabe, Y. Ran, T. Cao, L. Fu, D. Xiao, W. Yao, and X. Xu, Nature (London) **622**, 63 (2023).

[18] F. Xu, Z. Sun, T. Jia, C. Liu, C. Xu, C. Li, Y. Gu, K. Watanabe, T. Taniguchi, B. Tong, J. Jia, Z. Shi, S. Jiang, Y. Zhang, X. Liu, and T. Li, Phys. Rev. X **13**, 031037 (2023).

[19] Z. Lu, T. Han, Y. Yao, A. P. Reddy, J. Yang, J. Seo, K. Watanabe, T. Taniguchi, L. Fu, and L. Ju, Nature (London) **626**, 759 (2024).

[20] N. R. Chebrolu, B. L. Chittari, and J. Jung, Phys. Rev. B **99**, 235417 (2019).

[21] M. Koshino, Phys. Rev. B **99**, 235406 (2019).

[22] Y.-H. Zhang, D. Mao, Y. Cao, P. Jarillo-Herrero, and T. Senthil, Phys. Rev. B **99**, 075127 (2019).

[23] J. Liu, Z. Ma, J. Gao, and X. Dai, Phys. Rev. X **9**, 031021 (2019).

[24] B. L. Chittari, G. Chen, Y. Zhang, F. Wang, and J. Jung, Phys. Rev. Lett. **122**, 016401 (2019).

[25] J. Y. Lee, E. Khalaf, S. Liu, X. Liu, Z. Hao, P. Kim, and A. Vishwanath, Nat. Commun. **10**, 5333 (2019).

[26] M. König, S. Wiedmann, C. Brüne, A. Roth, H. Buhmann, L. W. Molenkamp, X.-L. Qi, and S.-C. Zhang, Science **318**, 766 (2007).

[27] C.-Z. Chang, J. Zhang, X. Feng, J. Shen, Z. Zhang, M. Guo, K. Li, Y. Ou, P. Wei, L.-L. Wang, Z.-Q. Ji, Y. Feng, S. Ji, X. Chen, J. Jia, X. Dai, Z. Fang, S.-C. Zhang, K. He, Y. Wang, L. Lu, X.-C. Ma, and Q.-K. Xue, Science **340**, 167 (2013).

[28] Y. Xia, D. Qian, D. Hsieh, L. Wray, A. Pal, H. Lin, A. Bansil, D. Grauer, Y. S. Hor, R. J. Cava, and M. Z. Hasan, Nat. Phys. **5**, 398 (2009).

[29] Y. L. Chen, J. G. Analytis, J.-H. Chu, Z. K. Liu, S.-K. Mo, X. L. Qi, H. J. Zhang, D. H. Lu, X. Dai, Z. Fang, S. C. Zhang, I. R. Fisher, Z. Hussain, and Z.-X. Shen, Science **325**, 178 (2009).

[30] T. Zhang, P. Cheng, X. Chen, J.-F. Jia, X. Ma, K. He, L. Wang, H. Zhang, X. Dai, Z. Fang, X. Xie, and Q.-K. Xue, Phys. Rev. Lett. **103**, 266803 (2009).

[31] A. L. Sharpe, E. J. Fox, A. W. Barnard, J. Finney, K. Watanabe, T. Taniguchi, M. A. Kastner, and D. Goldhaber-Gordon, Science **365**, 605 (2019).

[32] M. Serlin, C. L. Tschirhart, H. Polshyn, Y. Zhang, J. Zhu, K. Watanabe, T. Taniguchi, L. Balents, and A. F. Young, Science **367**, 900 (2020).

[33] G. Chen, A. L. Sharpe, E. J. Fox, Y.-H. Zhang, S. Wang, L. Jiang, B. Lyu, H. Li, K. Watanabe, T. Taniguchi, Z. Shi, T. Senthil, D. Goldhaber-Gordon, Y. Zhang, and F. Wang, Nature (London) **579**, 56 (2020).

[34] Y. Wang, J. Herzog-Arbeitman, G. W. Burg, J. Zhu, K. Watanabe, T. Taniguchi, A. H. MacDonald, B. A. Bernevig, and E. Tutuc, Nat. Phys. **18**, 48 (2022).

[35] B. Lian, F. Xie, and B. A. Bernevig, Phys. Rev. B **102**, 041402(R) (2020).

[36] Q. S. Wu, J. Liu, Y. Guan, and O. V. Yazyev, Phys. Rev. Lett. **126**, 056401 (2021).

[37] J. A. Crosse, N. Nakatsuji, M. Koshino, and P. Moon, Phys. Rev. B **102**, 035421 (2020).

[38] B. Lian, F. Xie, and B. A. Bernevig, Phys. Rev. B **103**, L161405 (2021).

[39] J. Herzog-Arbeitman, Z.-D. Song, N. Regnault, and B. A. Bernevig, Phys. Rev. Lett. **125**, 236804 (2020).

[40] M. He, Y. Li, J. Cai, Y. Liu, K. Watanabe, T. Taniguchi, X. Xu, and M. Yankowitz, Nat. Phys. **17**, 26 (2021).

[41] See Supplemental Material at http://link.aps.org/supplemental/10.1103/PhysRevLett.133.246401 which includes Refs. [42–45], for additional information about the experimental methods and theoretical calculations.

[42] C. R. Dean, A. F. Young, I. Meric, C. Lee, L. Wang, S. Sorgenfrei, K. Watanabe, T. Taniguchi, P. Kim, K. L. Shepard, and J. Hone, Nat. Nanotechnol. **5**, 722 (2010).

[43] R. Ribeiro-Palau, S. Chen, Y. Zeng, K. Watanabe, T. Taniguchi, J. Hone, and C. R. Dean, Nano Lett. **19**, 2583 (2019).

[44] A. C. Ferrari, J. C. Meyer, V. Scardaci, C. Casiraghi, M. Lazzeri, F. Mauri, S. Piscanec, D. Jiang, K. S. Novoselov, S. Roth, and A. K. Geim, Phys. Rev. Lett. **97**, 187401 (2006).

[45] B. A. Bernevig, T. L. Hughes, and S.-C. Zhang, Science **314**, 1757 (2006).

[46] P. Streda, J. Phys. C **15**, L1299 (1982).

[47] R. Bistritzer and A. H. MacDonald, Phys. Rev. B **84**, 035440 (2011).

[48] J. Yu, B. A. Foutty, Z. Han, M. E. Barber, Y. Schattner, K. Watanabe, T. Taniguchi, P. Phillips, Z.-X. Shen, S. A. Kivelson, and B. E. Feldman, Nat. Phys. **18**, 825 (2022).

[49] K. P. Nuckolls, M. Oh, D. Wong, B. Lian, K. Watanabe, T. Taniguchi, B. A. Bernevig, and A. Yazdani, Nature (London) **588**, 610 (2020).

[50] Y. Saito, J. Ge, L. Rademaker, K. Watanabe, T. Taniguchi, D. A. Abanin, and A. F. Young, Nat. Phys. **17**, 478 (2021).

[51] Y. Xie, A. T. Pierce, J. M. Park, D. E. Parker, E. Khalaf, P. Ledwith, Y. Cao, S. H. Lee, S. Chen, P. R. Forrester, K. Watanabe, T. Taniguchi, A. Vishwanath, P. Jarillo-Herrero, and A. Yacoby, Nature (London) **600**, 439 (2021).